(8a) and adjustments are made in the As and in the B_1 relative to B_2 to improve the agreement. This procedure is continued until the agreement is as close as possible. After obtaining a little experience on how changes in the As and Bs influence the $q_s(X, Y)/q_0$ it was possible to obtain very good agreement with less than 20 trials. The results are discussed in the next section.

RESULTS AND DISCUSSION

By letting the amplitude coefficient B_2 equal zero, the solution in equations (10a) and (10b) reduces to the two-dimensional case and can be compared with results obtained by conformal mapping in [1] and [2]. For each set of parameters $k(t_s - t_w)/wq_0$ and $q_s(X = 1)/q_0$, the coefficients A_1 and B_1 were adjusted, as outlined in the Analysis, until the heat flow boundary condition (8b) was satisfied as closely as possible. The factor A_1 gave sufficient freedom in the shape of the F function that the heating boundary condition could be matched very well for all the cases that were selected. The resulting solidification boundaries are shown in Fig. 2. The maximum deviations in matching (8b) occurred for $q_s(X = 1)/q_0 = 8$, which is an extreme variation in surface heat flux. In this instance the $q_s(X)/q_0$ curve never deviated from (8b) by more than about 3% of the total amplitude in the heat flux variation, and the solidification shapes in Fig. 2 are estimated to be accurate within a few percent. To verify the method, solidification shapes were first calculated for some of the parameters in [1] and excellent agreement was obtained.

For the two-dimensional solidification interfaces in Fig. 2, the A_1 and B_1 values are in Table 1, part (a). After the A_1 and B_1 were found for a few values of the parameters, it was not difficult to extrapolate to trial values of A_1 and B_1 for other cases. As expected physically, the shapes in Fig. 2 have smaller thicknesses in the regions of high interface heat flux. The thickness variations show the sensitivity of the interface to spatial variations in the convective heat transfer; this is of interest in showing how carefully the convection must be controlled in casting and crystal growing processes requiring that the interface be kept flat. The thickness variations are much less than by assuming locally one-dimensional heat flow through the region; in this instance the local thickness would be in inverse proportion to the heating if the interface is reasonably flat. The two-dimensional heat flow through the region tends to equalize the thickness variations required to accommodate to the nonuniform heat flux at the interface. This also aids the present solution method as the error in predicted thickness is usually much less than the error in matching the heat flow boundary conditions at the interface.

Three-dimensional solidification interfaces are shown in Fig. 3. for a square cross-section and for a rectangle with aspect ratio two. The A and B coefficients are in Table 1, part (b). Since the three-dimensional shape is appreciably more complex than for two dimensions, it is more difficult to match the surface heat flux variation (8a) in all details. Good heat flux matching was obtained for the parameters in Fig. 3; the accuracy decreased for $q_s(1, L)/q_0$ larger than 3, which is a range of rather extreme heat flux variations. The errors in matching the boundary conditions were somewhat less for $L = 2$ than for $L = 1$. It is estimated that for the case with the largest matching errors, $q_s(1, L)/q_0 = 3$ and $L = 1$, the thickness in Fig. 3(a) is about 7% too small in the region of the two corners $X = 1$, $Y = 0$, and $X = 0$, $Y = 1$. Since the results provide the sensitivity of the interface shape to the heating variations, small adjustments could have been made such as increasing the thickness in these corners by several percent, but this was not done for the shapes presented. The thicknesses at the origin $X = Y = 0$ and at the corner farthest from the origin have good accuracy as the interface heat fluxes were matched very well in these regions.

As in the two-dimensional case the local thickness reflects an inverse relation to the interface heat flux. As the $q_s(1, L)/q_0$ is increased, the total energy transferred through the solidified region is increased; hence, there is a decrease in the average region thickness. The examples in Fig. 3 illustrate the three-dimensional solidification shapes that can be evaluated from the analytical solution with very little computing effort.

REFERENCES

1. R. Siegel, Analysis of solidification interface shape resulting from applied sinusoidal heating, *J. Heat Transfer* **104,** 13–18 (1982).
2. R. Siegel and D. J. Sosoka, Cauchy integral method for two-dimensional solidification interface shapes, *Int. J. Heat Mass Transfer* **25,** 975–984 (1982).
3. R. H. Nilson and Y. G. Tsuei, Free boundary problem for the Laplace equation with application to ECM tool design, *J. appl. Mech.* **98,** 54–58 (1976).
4. G. H. Meyer, The method of lines and invariant imbedding for elliptic and parabolic free boundary problems, *SIAM J. Num. Anal.* **18,** 150–164 (1981).
5. J. Crank and T. Ozis, Numerical solution of a free boundary problem by interchanging dependent and independent variables, *J. Inst. Maths Appl.* **26,** 77–85 (1980).
6. R. Siegel and A. Snyder, Analysis of coolant entrance boundary shape of porous region to control cooling along exit boundary, *J. Heat Transfer* **105,** 513–518 (1983).

Int. J. Heat Mass Transfer. Vol. 28, No. 3, pp. 705–714, 1985
Printed in Great Britain

0017–9310/85 $3.00 + 0.00
Pergamon Press Ltd.

Flow patterns of natural convection in horizontal cylindrical annuli

YAN-FEI RAO, YASUTOMI MIKI, KENJI FUKUDA, YASUYUKI TAKATA and SHU HASEGAWA

Department of Nuclear Engineering, Faculty of Engineering, Kyushu University, Fukuoka 812, Japan

(*Received* 26 *March* 1984 *and in revised form* 31 *May* 1984)

NOMENCLATURE

D	diameter
g	gravitational acceleration
k	mesh constant in equation (6)
L	gap width of the annulus, $r_o - r_i$
Nc	number of nodal points in circumferential direction
Nu	mean Nusselt numbers
p	pressure
Pr	Prandtl number, $\mathrm{Pr} = \nu/\alpha$
r	radial distance
R	ratio of the outer to the inner radius, r_o/r_i
Ra	Rayleigh number based on the inner radius r_i, $g\beta(T_i - T_o)r_i^3/\alpha\nu$
Ra_L	Rayleigh number based on the gap width L

t time
T temperature
u, v velocity components in radial and circumferential direction, respectively
z axial coordinate.

Greek symbols
α thermal diffusivity
β thermal expansion coefficient
θ dimensionless temperature
ν kinematic viscosity
ϕ angular coordinate measured from down vertical
ψ stream function
ω vorticity.

Subscripts
i, o inner and outer
i, j grid numbers in radial and circumferential direction.

Superscripts
b outer iteration number
n time step number.

INTRODUCTION

NATURAL convection in concentric annuli has been a subject of interest to many investigators. The problem was first investigated experimentally by Beckmann [1] with air, hydrogen and carbon dioxide as the test fluids to obtain overall heat transfer coefficients. Liu *et al.* [2] measured the radial temperature profiles and the heat transfer coefficients using air, water and silicon, and showed that there existed a critical Rayleigh number at which the flow changed from a steady to an unsteady one. With smoke as a tracer, photographs of flow patterns in air were presented by Bishop *et al.* [3, 4], describing an oscillatory flow in detail. Grigull and Hauf [5] used a Mach–Zehnder interferometer to measure the local heat transfer coefficients in air on the inner cylinder for nine radius ratios; they found three different flow regimes of convection which were named the two-dimensional pseudo-conduction regime, the three-dimensional (3-D) spiral flow regime, and the fully developed two-dimensional (2-D) regime. In an experimental study by Powe *et al.* [6], the flow patterns of convection were investigated and the maximum Rayleigh numbers below which the flow was actually steady were given over a wide range of radius ratios. Powe *et al.* [7], in their later work, also presented an analytical study in which they regarded the appearance of any positive value of stream function as the sign of the secondary counter-rotating cells generation; thus, they determined indirectly the transition Grashof numbers since experimental evidence revealed that steady 2-D multiple cells were generated immediately after the transition. Kuehn and Goldstein [8] also investigated the problem experimentally and numerically. A Mach–Zehnder interferometer was used to determine the temperature distribution and the local heat transfer coefficients in air and water. With water, they demonstrated that the flow remained steady even though the Rayleigh number was well over the critical value obtained experimentally with air, which suggests that the Prandtl number affected the transition characteristics. Custer and Shaughnessy [9] investigated analytically the steady natural convection in a fluid of very low Prandtl number, using a technique of double perturbation expansion in powers of the Grashof and Prandtl numbers. Charrier-Mojtabi *et al.* [10] gave numerical solutions using the alternating direction implicit (ADI) method for three cases: a wide annulus ($R = 2, 2.6$) for $Pr = 0.7$, a narrow annulus ($R = 1.2$) for $Pr = 0.7$ and a wide annulus ($R = 2, 5$) for $Pr = 0.02$. On treating the problem numerically at high Rayleigh numbers, Jischke and Farshchi [11] divided the flow field of an annulus into five regions which include an inner boundary layer near the inner cylinder, an outer boundary layer near the outer cylinder, a vertical plume region above the inner cylinder, a stagnant region below the inner cylinder and a core region surrounded by these four regions; they applied the boundary layer approximation to obtain the temperature distribution and heat transfer rates. A numerical parametric study was carried out by Kuehn and Goldstein [12], in which the effects of the Prandtl number and the radius ratio on heat transfer coefficient were investigated. Farouk and Guceri [13] applied the k–ε turbulence model to study the turbulent natural convection for high Rayleigh numbers ranging from 10^6 to 10^7 with a radius ratio of 2.6. A comparison of Nusselt numbers between the results obtained numerically and those obtained experimentally by other investigators showed a good agreement. One of the latest numerical studies on this problem was conducted by Tsui and Tremblay [14], who presented the results of mean Nusselt numbers for both the transient or the steady natural convection.

As mentioned above, although many investigations have been carried out on this subject, there are only a few numerical studies treating the transient oscillatory phenomena and/or the 3-D ones observed experimentally. Especially, the numerical determination of the critical Rayleigh number at which the unsteady flow occurs still remains undone. In the present study, either the 3-D steady or the 2-D transient numerical analyses are carried out to simulate the convection in annuli. Experiments are also conducted to visualize the flow pattern. The temperature and/or the stream function distributions, thus obtained numerically and experimentally, are classified and compared with the flow pattern map after Powe *et al.*, predicting which flow pattern is dominant at a given Rayleigh number and radius ratio.

ANALYSIS

Formulation and numerical procedure

As the analysis of the steady 3-D natural convection is described in our previous paper [15], only the transient 2-D analysis is presented here. The problem under consideration is the 2-D laminar convection between two horizontal isothermal concentric cylinders. The geometry of the cylinders is shown in Fig. 1. The gap between the cylinders is filled with a viscous fluid, which is set in motion by the temperature difference across the annulus. The inner and the outer cylinders, of radii r_i and r_o, are maintained at different uniform temperatures T_i and T_o, respectively. The gravity force on the system exerts vertically downward. Cylindrical coordinates (r, ϕ, z) are utilized, where ϕ is measured from the down vertical, r from the axis and z along the axis. All quantities are assumed to be independent of z, and all fluid properties constant.

Then the governing equations are given in dimensionless forms as follows:

$$\frac{1}{Pr}\left[\frac{\partial \omega}{\partial t}+\frac{1}{r}\frac{\partial}{\partial r}(ru\omega)+\frac{1}{r}\frac{\partial}{\partial \phi}(v\omega)\right] = Ra\left(\sin\phi\frac{\partial\theta}{\partial r}+\cos\phi\frac{1}{r}\frac{\partial\theta}{\partial\phi}\right)+\nabla^2\omega \quad (1)$$

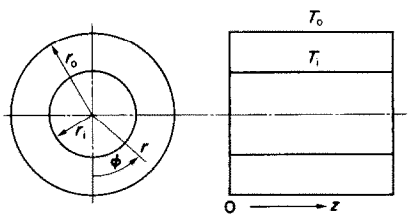

FIG. 1. Flow geometry and coordinate system.

$$\nabla^2\psi = -\omega \tag{2}$$

$$\frac{\partial\theta}{\partial t}+\frac{1}{r}\frac{\partial}{\partial r}(ru\theta)+\frac{1}{r}\frac{\partial}{\partial\phi}(v\theta)=\nabla^2\theta \tag{3}$$

where the definition of the stream function is

$$u=\frac{1}{r}\frac{\partial\psi}{\partial\phi},\qquad v=-\frac{\partial\psi}{\partial r}. \tag{4}$$

The boundary conditions are

$$\begin{aligned} u=v=\psi=0 \quad &\text{at} \quad r=1,R\\ \theta=1 \quad &\text{at} \quad r=1\\ \theta=0 \quad &\text{at} \quad r=R\\ \omega=-\frac{\partial^2\psi}{\partial r^2} \quad &\text{at} \quad r=1,R \end{aligned} \tag{5}$$

where R is the ratio of the radius of the outer cylinder to that of the inner cylinder.

These equations are solved by using the finite difference method, with the computer FACOM-200.

In an attempt to keep the convergence time to a minimum without sacrificing accuracy, a non-uniform mesh system is used for the geometry shown in Fig. 1, which can be described as

$$\Delta\phi_{j+1}=k\Delta\phi_j \quad (j=1,2,\ldots,Nc/2). \tag{6}$$

In equation (6), k is a constant value chosen appropriately to make the mesh grid coarse at the bottom and concentrated at the top of the annulus, where steep variations in the temperature and in the stream function are expected. Usually, the non-uniform mesh system is formed by dividing the domain into several regions of different mesh size, but it is noted that in such a mesh system the error for the central difference scheme is an order of $\Delta\phi$, at the boundary of the regions, instead of $\Delta\phi^2$ [16]. The advantage of the present over the conventional mesh system lies in that a truncation error of order $\Delta\phi^2$ may be kept for the central difference scheme, if the value of k is sufficiently close to unity so that $(k-1)$ will have an order of $\Delta\phi$. This is the actual case of our investigation. The derivative in the ϕ direction can be approximated by

$$\begin{aligned} \left(\frac{\partial F}{\partial\phi}\right)_{(i,j)} &= \frac{F_{i,j+1}+(k^2-1)F_{i,j}-k^2F_{i,j-1}}{(k+1)\Delta\phi_j}\\ \left(\frac{\partial^2 F}{\partial\phi^2}\right)_{(i,j)} &= 2\times\frac{F_{i,j+1}-(k+1)F_{i,j}+kF_{i,j-1}}{(k+1/k)\Delta\phi_j^2} \end{aligned} \tag{7}$$

where i and j denote the grid number in the r and ϕ directions, respectively.

For given Ra, Pr and R, the non-linear equations (1)–(3) are solved iteratively within each time step as follows. Equation (1) is first solved to obtain the vorticity field with the ADI scheme; second, the vorticity values obtained are used to calculate the stream function by equation (2) with the SOR method; and finally, equation (3) is solved with the ADI scheme to obtain the temperature distribution. Thus the one step of iteration, the outer iteration, is completed. After each iteration the convergence test is performed to determine whether to proceed to the next time step or to continue more iterations. The test for the convergence of an interation involves calculating the absolute value of the maximum relative difference between two consecutive iterations, and comparing it with prescribed constants. The conditions are stated as

$$\begin{aligned} \max\left|\frac{\omega^b_{i,j,n}-\omega^{b-1}_{i,j,n}}{\omega^b_{i,j,n}}\right| &< \varepsilon_1\\ \max\left|\frac{\psi^b_{i,j,n}-\psi^{b-1}_{i,j,n}}{\psi^b_{i,j,n}}\right| &< \varepsilon_2\\ \max\left|\frac{\theta^b_{i,j,n}-\theta^{b-1}_{i,j,n}}{\theta^b_{i,j,n}}\right| &< \varepsilon_3 \end{aligned} \tag{8}$$

where b denotes the number of outer iterations, and ε_1, ε_2 and ε_3 are set to 10^{-3}. The mean Nusselt numbers, Nu_i and Nu_o, are defined as follows:

$$\begin{aligned} Nu_i &= \frac{1}{2\pi}\int_0^{2\pi} -\ln R\left(\frac{\partial\theta}{\partial r}\right)_{r=1} d\phi,\\ Nu_o &= \frac{1}{2\pi}\int_0^{2\pi} -R\ln R\left(\frac{\partial\theta}{\partial r}\right)_{r=R} d\phi. \end{aligned} \tag{9}$$

RESULTS AND DISCUSSION

Accuracy of calculation

Numerical calculations were performed successfully over a wide range of Rayleigh numbers and aspect ratios for $Pr = 0.7$ and 5000. Figure 2 shows the conditions for calculation in a chart similar to that used by Powe *et al.* [6], with the inverse relative gap width as abscissa.

In order to make a simple check of the numerical scheme, the mean Nusselt numbers obtained numerically are compared against experimental results in the lower part of Fig. 3 with a characteristic length of $\sqrt{(r_i\times r_o)}\ln(r_i/r_o)$, which was first introduced by Itoh *et al.* [17] to include the effect of aspect ratio. A reasonable consistency can be found between the numerical solutions and Itoh's correlation, except that a slight effect of aspect ratio still remains in our calculations. Comparing our results directly with Grigull's experimental data with a close range of aspect ratio to ours, we discover excellent agreement, as shown in the upper part of Fig. 3.

The convergence, as well as the accuracy, of the numerical method are also checked by comparing mean Nusselt numbers at the inner and the outer cylinders, as done by many investigators. However, there are usually comparatively large disagreements between the two values, especially at high Rayleigh numbers. A disagreement of 9% is estimated in the case of $Ra_L = 10^5$, $R = 2.6$, for numerical results presented by Kuehn and Goldstein [8]. Also, a recent study by Tsui and Tremlay [14] showed the disagreement "within 5%". Unlike these, in our present investigation, Nu_i and Nu_o approach the same steady state value as t increases if a steady state exists; the difference between the two is almost zero even for a Rayleigh number higher than those referred to above. The mean Nusselt numbers at the inner and outer cylinders obtained numerically are shown in Fig. 4, where it is found that they approach, as time elapses, 5.7835 and 5.7688, respectively, with a relative difference of 0.25%. This is the same order as the inherently existing error of the finite difference approximation.

Flow pattern and temperature distribution

In addition to the ordinary 2-D stable unicellular flow pattern for relatively low Rayleigh numbers, Powe *et al.* [6]

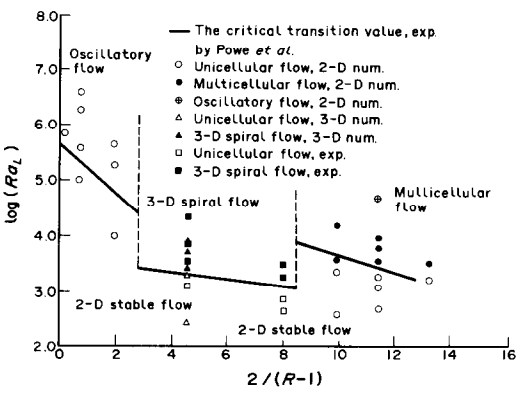

FIG. 2. Flow pattern chart.

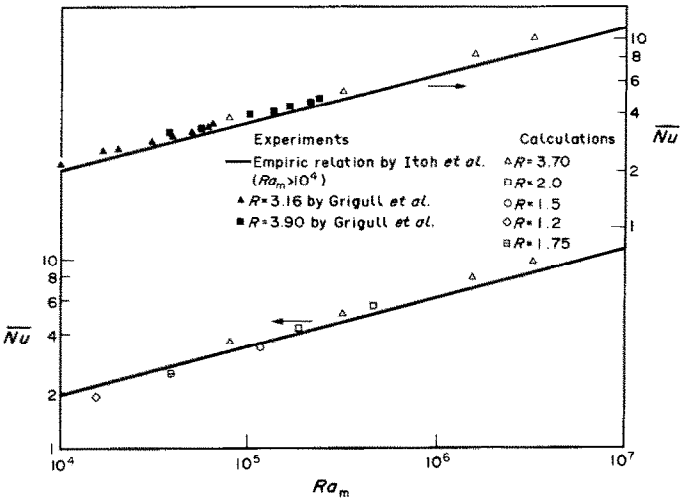

FIG. 3. Steady state mean Nusselt numbers.

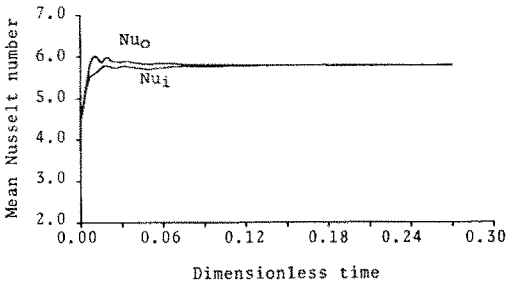

FIG. 4. Transient mean Nusselt numbers for $Ra_L = 5 \times 10^5$, $Pr = 0.7$, $R = 2.0$.

observed three different unsteady flow patterns which occurred at relatively high Rayleigh numbers depending on the inverse relative gap width. These are, as they termed, a 2-D multicellular flow, a 3-D spiral flow and a 2-D oscillatory flow. Our numerical analyses, therefore, aim at simulating these three flow patterns at relatively high Rayleigh numbers, and the results are discussed individually according to the range of the aspect ratios in which each flow pattern prevails.

(1) *Narrow annulus for* $2/(R-1) > 8.5$. As revealed by experiments [2, 6], the stable crescent unicellular flow pattern changes into the multicellular flow pattern when the Rayleigh number exceeds a critical value, and by increasing the Rayleigh number, the flow comes to oscillate in such a way that small eddies periodically swing right and left at the upper part of the annulus. Figure 5 shows the flow patterns at Rayleigh numbers just below and above the transition critical Rayleigh number given by Powe *et al.* [6]. The flow pattern depicted in Fig. 5(a), known as the crescent-shaped flow pattern, is the most common one which can be observed over the whole range of aspect ratios. The temperature distribution in this case is like a family of concentric circles or a pseudo-conduction distribution. Figure 5(b), on the other hand, shows the typical multicellular flow pattern which appears just above the transition Rayleigh number. One may observe a pair of small counter-rotating cells built upon the main flow cell near the top of the annulus. This is in contrast to the numerical results obtained by Charrier-Mojtabi *et al.* [10] using the ADI method, in which they reported a failure to simulate the multicellular flow pattern, despite calculations with several initial conditions. Of course, the reason for this is uncertain; but it seems, from our experience, that the boundary condition of symmetry with respect to the center vertical, or a too coarse

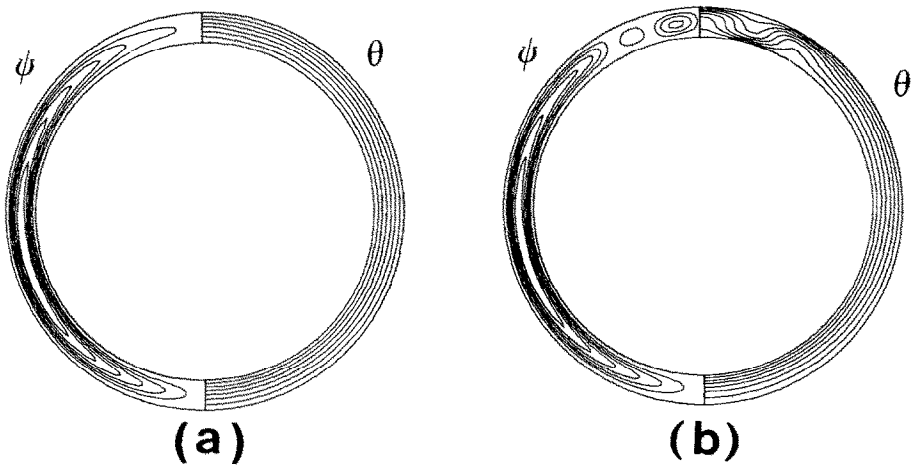

FIG. 5. Flow patterns of the narrow annulus for $Pr = 0.7$, $R = 1.175$: (a) $Ra_L = 2000$, (b) $Ra_L = 4000$.

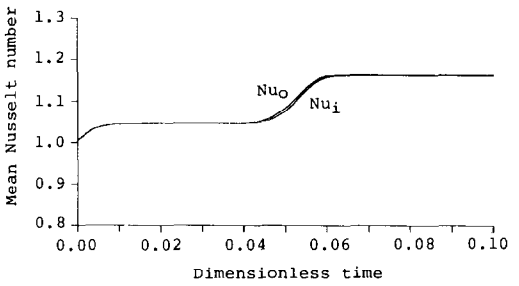

FIG. 6. Transient mean Nusselt numbers for $Ra_L = 4000$, $Pr = 0.7$, $R = 1.175$; initial condition: steady state solutions for $Ra_L = 2000$.

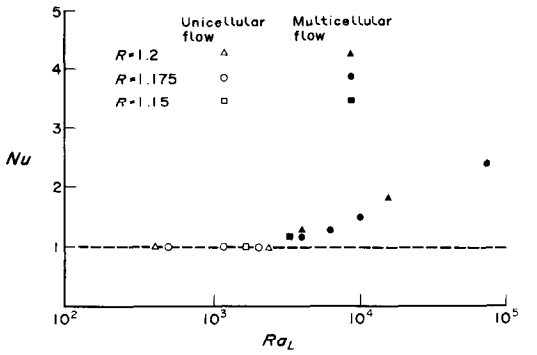

FIG. 7. Steady state mean Nusselt numbers in the narrow annulus.

mesh grid at the upper part of the annulus, or a too large time step, will not produce a good simulation of the multicellular flow pattern. Though several initial conditions were utilized in the present investigation, including a pure conduction solution, a homogeneous temperature distribution and a steady state solution for either a unicellular or a multicellular flow pattern, they had no effect on the ultimate results. This is different from the case for spheres [18].

Figure 6 shows a transient variation of mean Nusselt numbers, suggesting a transition of flow patterns from a unicellular to a multicellular mode. As the initial condition, the solution for a low Rayleigh number corresponding to Fig. 5(a) is used. Then a step change in Rayleigh number is imposed at time zero to obtain the ultimate flow pattern as shown in Fig. 5(b). As for Fig. 6, it is interesting to note that there are two stages at which different mean Nusselt numbers correspond, and that the changes do not always occur at the beginning but at a certain time when the flow pattern begins to change. Until then, for a rather long period, the mean Nusselt numbers are almost constant. Thus it may be assumed that two different steady state solutions with different Nusselt numbers exist, each corresponding to one of the stages in Fig. 6.

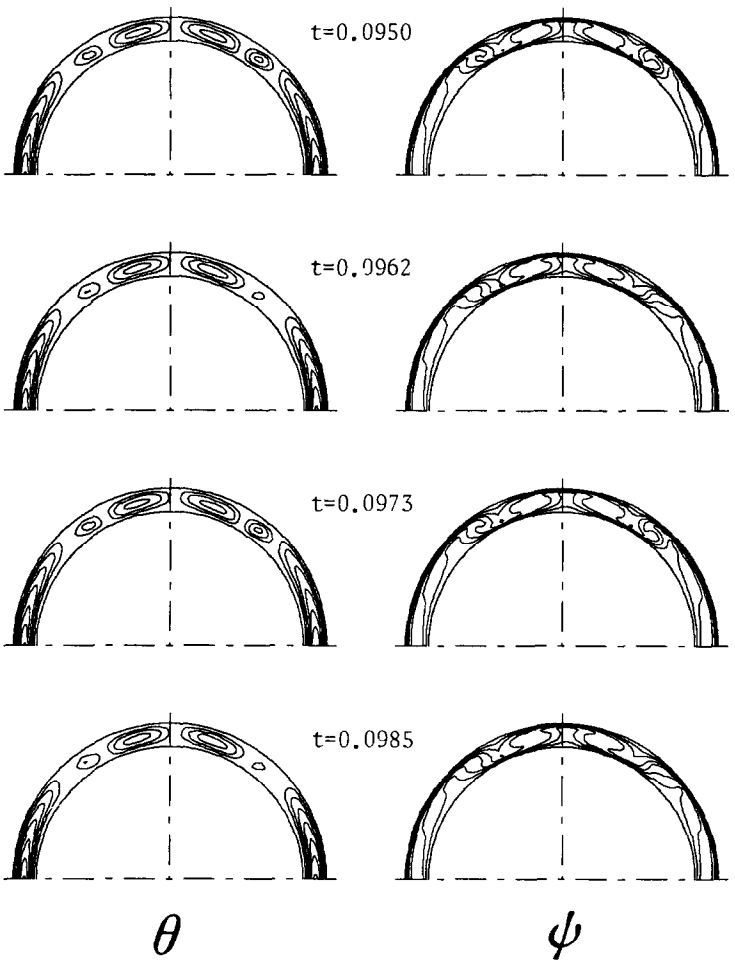

FIG. 8. Oscillatory flow in a narrow annulus for $Ra_L = 5 \times 10^4$, $Pr = 0.7$, $R = 1.175$.

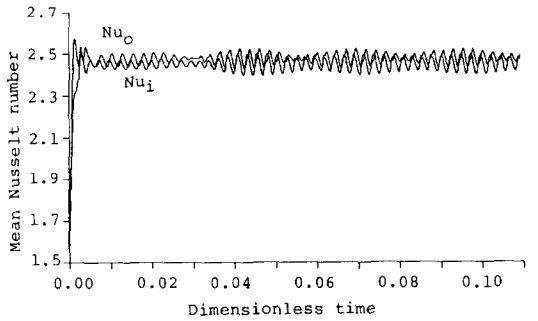

FIG. 9. Oscillation in mean Nusselt numbers for $Ra_L = 5 \times 10^4$, $Pr = 0.7$, $R = 1.175$.

The steady state mean Nusselt numbers are plotted against the Rayleigh numbers with radius ratios as a parameter in Fig. 7. It is found that unicellular flow patterns with a pseudoconduction temperature distribution dominate at low Rayleigh numbers; once the flow pattern becomes multicellular, the temperature distribution is affected causing the Nusselt numbers to deviate from those for pseudoconduction.

The cases calculated over this range of aspect ratios are plotted in Fig. 2 and the transition Rayleigh numbers are compared with those illustrated by Powe *et al.* [6]. Although the agreement is satisfactory, the boundary of the multicellular region obtained numerically shows some discrepancy. This situation, however, is the same as that faced by Powe *et al.* [7] in their numerical works; they attributed these discrepancies to the lack of experimental data in this region.

For high Rayleigh numbers, oscillatory flow patterns appear; an example is shown in Fig. 8. One may observe two small cells changing their sizes alternatively and regularly at the upper part of the annulus. The effect of this flow oscillation on mean Nusselt numbers is shown in Fig. 9. It is noted that the mean Nusselt numbers of the inner and outer cylinders have a slight relative difference of about 1%, and that there is no considerable effect on the mean Nusselt numbers because the oscillation is restricted to a limited part of the annulus.

(2) *Annulus with moderate gap for* $2.8 < 2/(R-1) < 8.5$. Since the appearance of the 3-D convective flow is reported [6] for this region of aspect ratios, steady 3-D numerical analysis is carried with the successive over-relaxation (SOR) method.

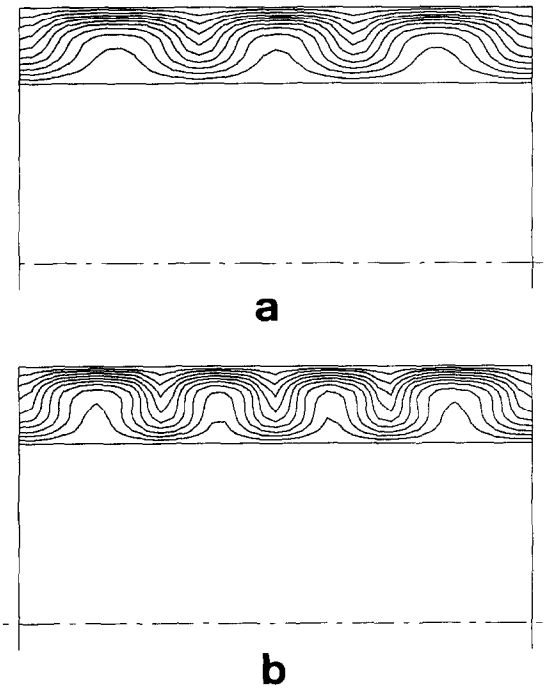

FIG. 11. Isotherms on the vertical symmetrical plane for $Pr = 5000$, $R = 1.428$: (a) $Ra_L = 2700$, (b) $Ra_L = 5400$.

The results are obtained for a fixed radius ratio of 1.428 with Rayleigh numbers (based on L) ranging from 1500 to 8100. It is found that the flow is 2-D unicellular at lower Rayleigh numbers, while it becomes 3-D spiral at Rayleigh numbers above 2700, confirming the map given by Powe *et al.* [6] in spite of the difference in Prandtl numbers: we chose 5000 in our analysis while it was close to unity in Powe's experiments. Figure 10 shows a typical 3-D spiral flow pattern. In the case of a Rayleigh number slightly above the critical transition value, the streak lines are almost parallel except at the upper region, where they form vortices. The annulus is divided into several zones each having a 3-D flow structure with such a vortex at its top, as is found and sketched by Grigull *et al.* [5] using air. It is

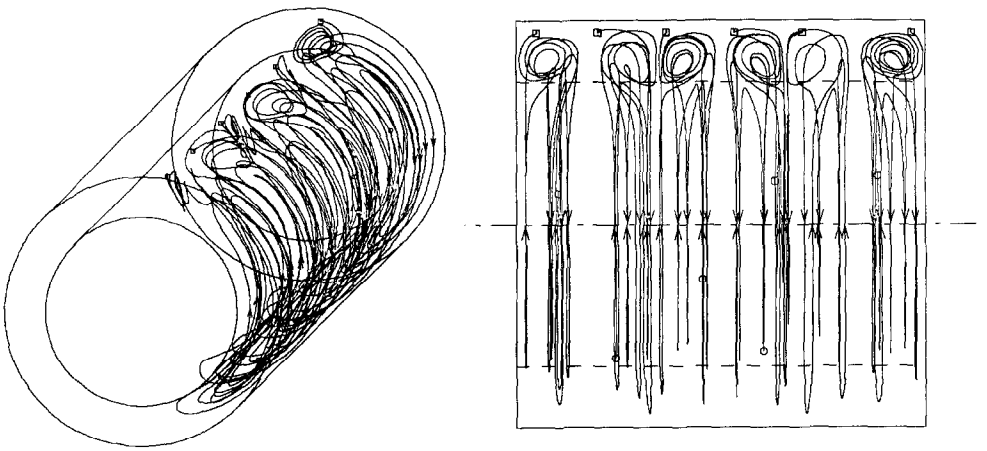

FIG. 10. Streak lines in the annulus with moderate gap for $Ra_L = 2700$, $Pr = 5000$, $R = 1.428$.

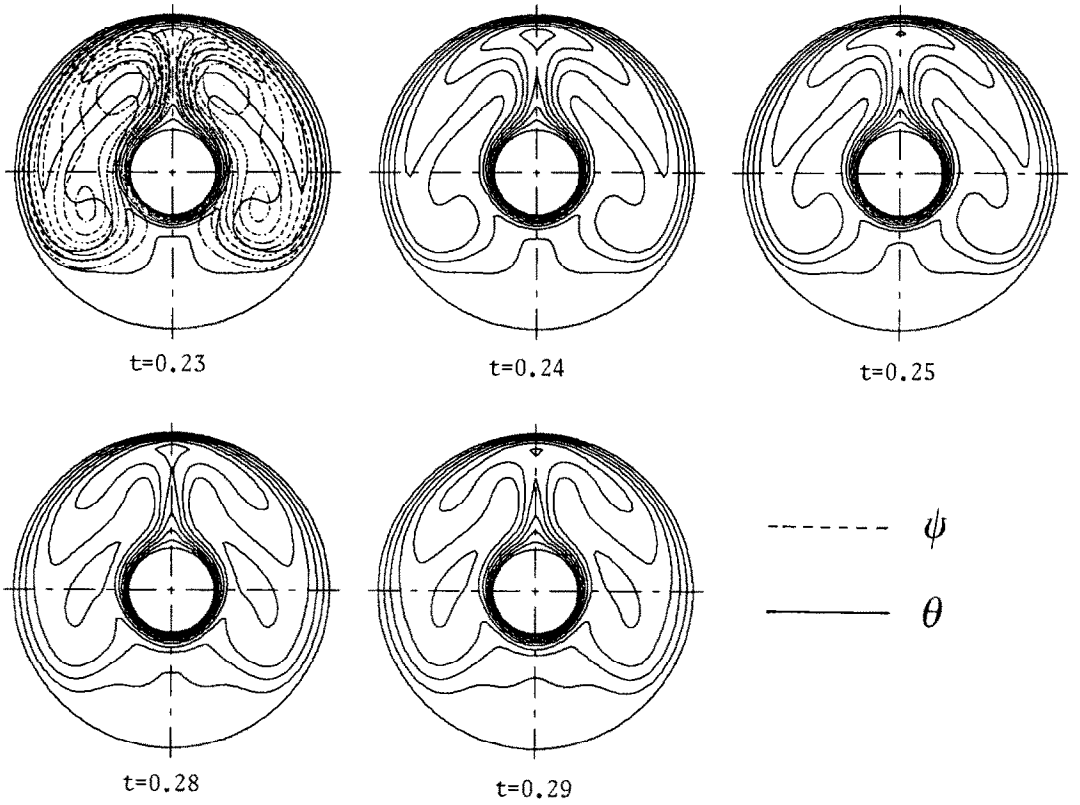

FIG. 12. Fluctuating phenomenon above the inner cylinder in the annulus with wide gap for $Ra_L = 1.0 \times 10^5$, $Pr = 0.7$, $R = 3.7$.

to be noted that this flow pattern is basically a row of transverse rolls often-observed in the rectangular box. It is found that the nature of the flow depends not only on the geometry, but also on the Rayleigh number, and that the number of vortices tends to increase as the Rayleigh number increases. Figure 11 shows the isotherms projected on the vertical symmetrical plane in which six and eight vortices are discriminated for Rayleigh numbers (based on L) 2700 and 5400, respectively.

(3) *Annulus with wide gap for* $2/(R-1) < 2.8$. An interesting oscillation in this range of aspect ratios was reported by some investigators [2, 4, 6] and examined in detail by Powe *et al.* [4]. In the present work, efforts were made to simulate this phenomenon; unfortunately, only steady state symmetrical solutions were obtained, even though the Rayleigh number was increased much higher than the transition one determined experimentally by Powe *et al.* [4, 6]. Unlike the case of a narrow annulus, in which the solutions are usually

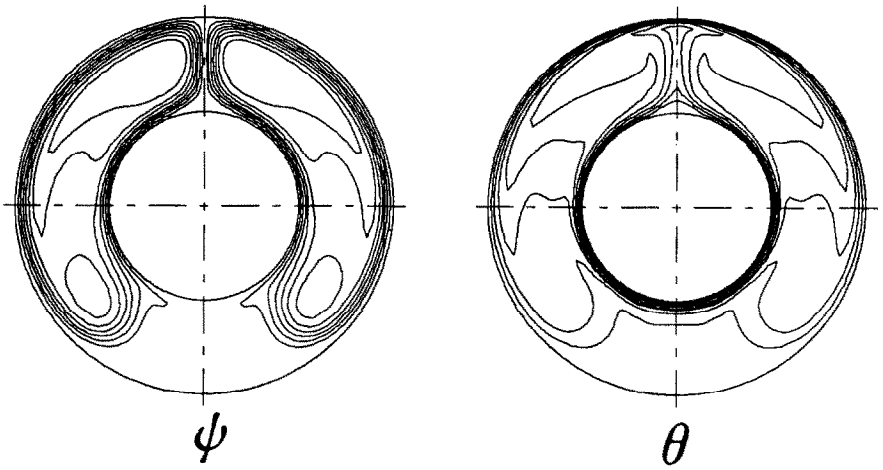

FIG. 13. Flow pattern at high Rayleigh number in the annulus with wide gap for $Ra_L = 5 \times 10^5$, $Pr = 0.7$, $R = 2.0$.

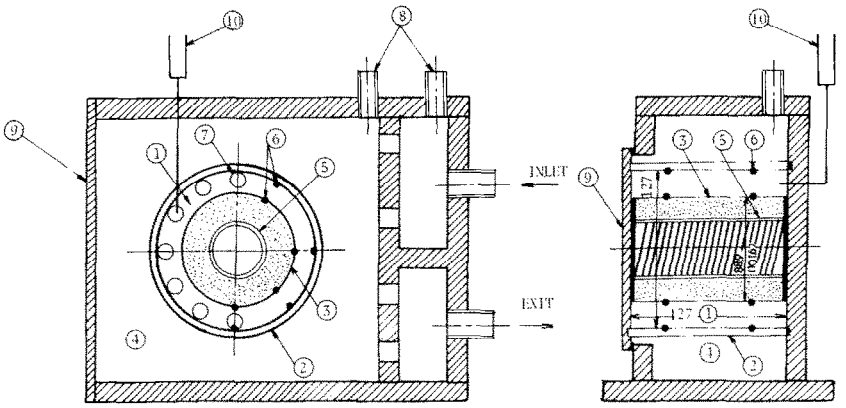

FIG. 14. Experimental apparatus: (1) test section, (2) outer cylinder, (3) inner cylinder, (4) water jacket, (5) heater, (6) thermocouples, (7) rubber corks, (8) rubber corks, (9) viewing window, (10) venting capillary.

asymmetrical slightly for Rayleigh numbers higher than the transition one, the symmetry is so pervasive that one might expect to obtain the same results even by performing calculations for only half of the annulus. Figure 12 shows a fluctuating phenomenon occurring just above the inner cylinder where thermal disturbances ascend consecutively. This phenomenon is also observed in a rectangular box of porous material heated from the middle half of its base [19]. In the present case, however, the fluctuation only lasts during a certain period, after which it diminishes to nothing. Figure 13 shows a flow pattern at the same Rayleigh number as that in Fig. 4, where one may deduce from either isotherms or streak lines that two boundary layers are formed on the cylinder surfaces, except at the upper part near the inner and the lower part near the outer surfaces.

EXPERIMENTAL

Apparatus and procedure

The side views of the experimental apparatus provided for the visual study are shown in Fig. 14. The apparatus consists of a fixed 127 mm i.d. and 127 mm long Pyrex outer tube to which either of two different aluminium inner tubes of 88.9 mm or 101.6 mm o.d. is assembled, resulting in radius ratios of 1.428 and 1.25, respectively. An electric heater made of 0.6 mm o.d.

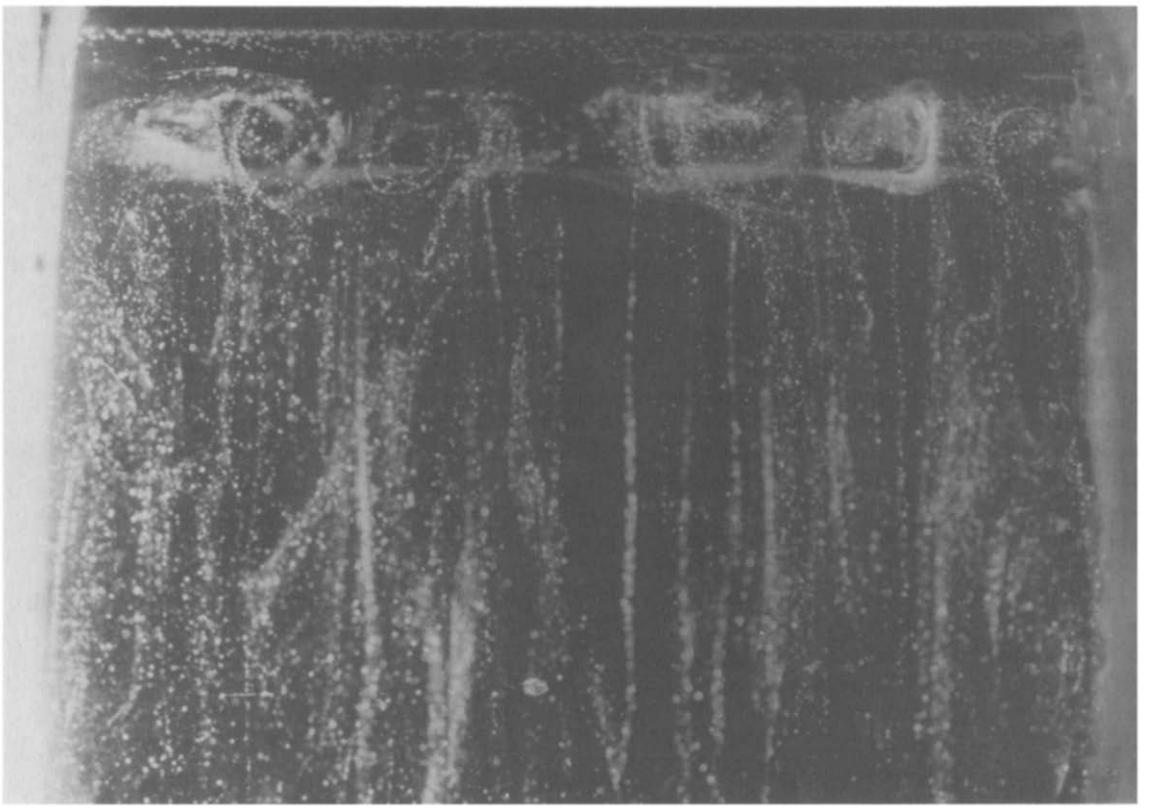

FIG. 15. Flow pattern for $Ra_L = 3500$, $Pr = 11\,700$, $R = 1.428$.

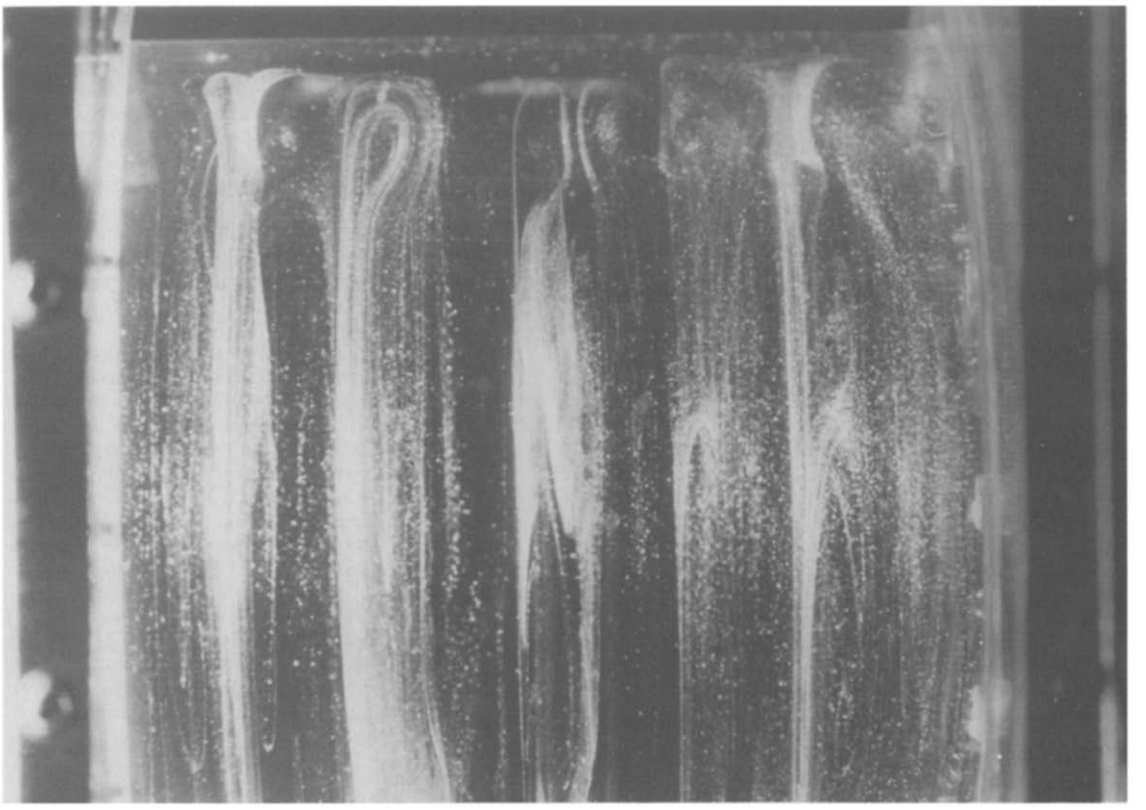

FIG. 16. Flow pattern for $Ra_L = 8100$, $Pr = 8300$, $R = 1.428$.

nichrom wire wrapped around a bakelite rod is inserted in the inner tube. The outer surface of the inner tube is coated with flat black paint to prevent reflection of light for photographic purposes. The whole system is immersed in a water jacket so that the outer tube is cooled to keep the tube surface temperature uniform. Chromel–alumel thermocouples are embedded in both tube walls at several axial and circumferential locations to measure the surface temperatures. Glycerol is used as the working fluid. Through the rubber corks attached to the acrylic resin end-plates, a tracer, aluminium powder, is slowly introducted with a long injector. To avoid thermal disturbances in the system, the tracer is mixed with Glycerol at the same temperature as in the system. Attaining steady state usually required 24 h after the heating power was increased to a prescribed value.

Results and comparison with analysis

One of the objectives of the present visualization study is to confirm the complex structure of the 3-D flow pattern obtained numerically. A photograph taken at the same condition as that for the analysis shown in Fig. 10 is given in Fig. 15. It is found that the tracers injected into the annulus at the lower part move upward along the inner cylinder and separate from it at the upper part to form several vortices. Comparing this with Fig. 10, one may observe the close similarity in flow patterns and even in the number of vortices. The trend of cell numbers to increase with Ra, which was predicted by the analysis, is confirmed experimentally. A photograph in Fig. 16 indicates the existence of eight cells in the case of a higher Rayleigh number than that for Figs 10 or 15. Like the results using air by Powe *et al.* [6], the flow patterns of a high viscous fluid (Glycerol) for this range of aspect ratios are also classified into the 2-D unicellular and the 3-D spiral flow pattern; the transition Rayleigh number is consistent with that estimated in our analysis and also with that shown in Powe's map. It seems that this transition is only dependent on geometry and not on Prandtl number. This trend varies greatly from the case of the transition to an oscillatory 2-D flow in an annulus with wide gap, which is reported to be dependent on both the geometry and Prandtl number [2, 8]. It is considered that this difference results mostly from the fact that the transition for this region occurs at very low Rayleigh numbers under the condition near a pseudoconduction one, so that the effect of the Prandtl number disappears.

CONCLUSIONS

Numerical and experimental investigations into natural convective flows in horizontal concentric annuli are presented. Emphases are placed on realizing analytically and experimentally various flow patterns which have been indicated in Powe's experimental map [6]. By 2-D and 3-D calculations over a wide range of Rayleigh numbers and aspect ratios, together with the visualization experiment, the general trend presented by Powe *et al.* [6] is confirmed except for the case of a wide annulus. For a narrow annulus, the region where multicellular flow pattern appears and the transition Rayleigh number given by Powe *et al.* [6] are consistent with our results. But, by further increases in Ra, our results show that an interesting oscillative flow is generated at the upper part of the annulus which nonetheless has little affect on the mean Nusselt numbers. It seems that complementary experiments are required to confirm this phenomenon. In the case of the annulus with a moderate gap, the structure of the 3-D spiral flow, which Grigull and Hauf [5] clarified experimentally, is also confirmed. In the case of the large annulus we failed to realize the oscillatory 2-D flow analytically even when the

Rayleigh number was higher than the transition Rayleigh number given by Powe *et al.* [6]. However, as other work [4] suggests that this phenomenon is not two-dimensional but three-dimensional, it presumably is necessary to perform the transient 3-D analysis to simulate it.

Acknowledgements—The authors would like to express their appreciation to Mr. Masataka Hidaka for his help in experiments. Also, the authors are grateful for the support of the Computing Center of Kyushu University.

REFERENCES

1. W. Beckmann, Die Warmeubertragung in zylindrischen Gasschichten bei naturlicher Konvektion, *Forsch. Geb. d. Ingenieurwesen* **2,** 165–178 (1931).
2. C. Y. Liu, W. K. Mueller and F. Landis, Natural convection heat transfer in long horizontal cylindrical annuli, *Int. Devl. Heat Transfer* **V,** 976–984 (1961).
3. E. H. Bishop and C. T. Carley, Photographic studies of natural convection between concentric cylinders, *Proc. 1966 Heat Transfer Fluid Mech. Inst.* 63–78 (1966).
4. E. H. Bishop, C. T. Carley and R. E. Powe, Natural convective oscillatory flow in cylindrical annuli, *Int. J. Heat Mass Transfer* **11,** 1741–1752 (1968).
5. U. Grigull and W. Hauf, Natural convection in horizontal cylindrical annuli, *Proc. 3rd Int. Heat Transfer Conf.* **2,** 182–195 (1966).
6. R. E. Powe, C. T. Carley and E. H. Bishop, Free convective flow patterns in cylindrical annuli, *J. Heat Transfer* **91,** 310–314 (1969).
7. R. E. Powe, C. T. Carley and S. L. Carruth, A numerical solution for natural convection in cylindrical annuli, *J. Heat Transfer* **92,** 210–220 (1971).
8. T. H. Kuehn and R. J. Goldstein, An experimental and theoretical study of natural convection in the annulus between horizontal concentric cylinders, *J. Fluid Mech.* **74,** 695–719 (1976).
9. J. R. Custer and E. J. Shaughnessy, Thermoconvective motion of low Prandtl number fluids within a horizontal cylindrical annulus, *J. Heat Transfer* **99,** 596–601 (1977).
10. M. C. Charrier-Mojtabi, A. Mojtabi and J. P. Caltagirone, Numerical solution of a flow due to natural convection in horizontal cylindrical annulus, *J. Heat Transfer* **101,** 171–173 (1979).
11. M. C. Jischke and M. Farshchi, Boundary layer regime for laminar free convection between horizontal circular cylinders, *J. Heat Transfer* **102,** 228–235 (1980).
12. T. H. Kuehn and R. J. Goldstein, A parametric study of Prandtl number and diameter ratio effects on natural convection heat transfer in horizontal cylindrical annuli, *J. Heat Transfer* **102,** 768–770 (1980).
13. B. Farouk and S. I. Guceri, Laminar and turbulent natural convection in the annulus between horizontal concentric cylinders, *J. Heat Transfer* **104,** 631–636 (1982).
14. Y. T. Tsui and B. Tremblay, On transient natural convection heat transfer in the annulus between concentric, horizontal cylinders with isothermal surfaces, *Int. J. Heat Mass Transfer* **27,** 103–111 (1984).
15. Y. Takata, K. Iwashige, K. Fukuda and H. Hasegawa, Three-dimensional natural convection in an inclined cylindrical annulus, *Int. J. Heat Mass Transfer* **27,** 747–754 (1984).
16. P. J. Roache, *Computational Fluid Dynamics*, Chap. 6. Hermosa Publishers (1976).
17. M. Itoh, T. Fujita, N. Nishiwaki and M. Hirata, A new method of correlating heat-transfer coefficients for natural convection in horizontal cylindrical annuli, *Int. J. Heat Mass Transfer* **13,** 1364–1368 (1970).
18. J. P. Caltagirone, M. Combarnous and A. Mojtabi, Natural convection between two concentric spheres: transition toward a multicellular flow, *Num. Heat Transfer* **3,** 107–114 (1980).
19. R. N. Horne and M. J. O'Sullivan, Origin of oscillatory convection in a porous medium heated from below, *Phys. Fluids* **21,** 1260–1264 (1978).

Int. J. Heat Mass Transfer. Vol. 28, No. 3, pp. 714–717, 1985
Printed in Great Britain

0017-9310/85 $3.00 + 0.00

Deflection of a circular jet by a weak cross-flow

P. M. STEFFLER and N. RAJARATNAM
Department of Civil Engineering, University of Alberta, Edmonton, Canada T6G 2G7

(*Received* 3 *October* 1983 *and in revised form* 26 *June* 1984)

NOMENCLATURE

- b transverse length scale (also used as length scale for other directions)
- f function
- g function
- I constant
- K numerical constant
- U ambient longitudinal velocity
- U_0 initial jet velocity
- u longitudinal velocity
- u_m maximum jet velocity at a section
- V ambient lateral velocity
- v lateral velocity
- w vertical velocity
- x longitudinal coordinate
- y lateral coordinate
- z vertical coordinate.

Greek symbols
- α ratio of initial jet velocity to cross-stream velocity
- ζ non-dimensional vertical coordinate
- η non-dimensional lateral coordinate
- θ momentum thickness
- ρ fluid density
- τ shear stress.

INTRODUCTION

THE PROBLEM of predicting the trajectory of a jet injected into a moving ambient fluid is of much importance and has been extensively studied both theoretically and experimentally. The authors have recently developed a simple method for the calculation of the deflection of a plane non-buoyant jet issuing